Scattering to Higher Harmonics for Quarter Wave and Helmholtz Resonators

K. Förner, J. Tournadre†‡, P. Martínez-Lera†, and W. Polifke

Professur für Thermofluiddynamik, Technische Universität München

Boltzmannstr. 15, 85748 Garching b. München, Germany

†Siemens Industry Software

Researchpark 1237, Interleuvenlaan 68, 3001 Leuven, Belgium

‡KU Leuven, Dept. of Mechanical Engineering

Celestijnenlaan 300B, 3001 Leuven, Belgium

The nonlinear response of acoustic resonators is investigated over a broad range of frequencies and amplitudes. Helmholtz resonators with a symmetric and with an asymmetric neck, respectively, as well as quarter wave resonators are considered. Describing functions for impedance and reflection coefficient of a Helmholtz resonator at various sound pressure levels are determined from compressible flow simulation and validated against experimental data. The particular focus of the present study is the nonlinear scattering to higher harmonics. For the Helmholtz resonator with a symmetric neck, a distinct pattern in the amplitudes of the higher harmonics is observed, where the odd harmonics dominate the response, while the even harmonics are almost negligible. Such an "Odd-Harmonics-Only" (OHO) pattern, which was observed previously in experiment at orifices, is explained by a quasi-steady analysis based on the Bernoulli equation, assuming a symmetric flow pattern at the neck. For the Helmholtz resonator with an asymmetric neck, it is observed in CFD simulations that even harmonics contribute noticeably to the resonator response, such that

the OHO pattern is less pronounced. For the markedly asymmetric geometry of the quarter wave resonator, the second harmonic is dominant and the OHO pattern vanishes completely. The quasi-steady analysis is extended successfully to describe also nonlinear scattering to higher harmonics for asymmetric configurations and flow patterns. Overall, the scattering to higher harmonics remains on a moderate level even at very high excitation levels for the Helmholtz resonator configurations. For the quarter wave resonator, the scattering is more pronounced and contributes perceptibly to the response at high excitation amplitudes.

Nomenclature

A_0 Cross-section area of the orifice, m^2

A_f, A_u Input amplitudes, m/s

c_0 Speed of sound, m/s

C_d Contraction factor, –

d_0 Neck diameter and quarter wave resonator diameter, m

d_{cav} Back-cavity diameter, m

f, g Riemann invariants, m/s

i Imaginary unit $\sqrt{-1}$, –

l_0 Neck thickness and quarter wave resonator length, m

l_c Reference length defined in Eq. (4), m

l_{cav} Back-cavity length, m

l_{ch} Chamfer length, m

l_e Effective length, m

p Pressure, Pa

p_{ref} Reference pressure for the calculation of the SPL, $20\,\mu$Pa

p_{rms} Root mean square of the overall pressure, Pa

p_c Reference pressure defined in Eq. (3), Pa

R Reflection coefficient, –

t Time, s

t_c Reference time defined in Eq. (3), s

u' Fluctuating velocity in the resonator tube, m/s

u'_0 Fluctuating velocity in the neck, m/s

Z, z Acoustic impedance (non-normalized and normalized), Rayl / –

Conventions

ODE Ordinary differential equation

OHO "Odd-harmonics-only" pattern

SPL Sound pressure level, dB

Symbols

Δp Pressure loss, Pa

ω_0 Fundamental angular frequency, rad/s

ω_{eig} Resonator angular eigenfrequency, rad/s

ϕ Acoustic velocity potential, m^2/s

ρ_0 Density, kg/m^3

σ Open area ratio, –

Superscripts

$\tilde{\bullet}$ Nondimensional quantity

$\bullet^{AJ}$ Quantity corresponding to the area jump

$\bullet^{HR}$ Quantity corresponding to the Helmholtz resonator

$\bullet^{QW}$ Quantity corresponding to the quarter wave resonator

$\hat{\bullet}$ Fourier transformed variable

$\bullet'$ Acoustic fluctuating part of the variable

I. Introduction

ACOUSTIC resonators are used in various industrial applications to reduce sound emission[1] or to avoid thermoacoustic instabilities[2,3]. Two basic types of such resonators are the Helmholtz and the quarter wave resonators[4], which are sketched in Fig. 1.

The scattering behavior of such resonators is investigated in this study under ambient conditions without mean flow. During operation in industrial applications, the scattering behavior of resonators can be strongly influenced by the working conditions. Some of these influencing effects are listed here. In most applications, a grazing flow over the resonators is present. This can cause a shift in the resonator eigenfrequency and has an impact on the resistance. This has been studied, e. g., experimentally by Jones *et al.*[5] and numerically by Zhang and Bodony[6]. Especially in gas turbines, resonators are often purged to guard them from the hot gas in the combustion chamber and to guarantee constant working conditions. Moreover, this increases the acoustic losses significantly, see for instance Eldredge and Dowling[7], Bellucci *et al.*[8], or Scarpato *et al.*[9]. When the amplitude of the acoustic excitation rises and the purging flow rate is too low, hot gas can penetrate the resonator opening. This can detune the resonator and should thus be avoided, see e. g., the studies by Ćosić *et al.*[10] and Rupp *et al.*[11].

The present study will be based on two approaches: computational fluid dynamics (CFD)

and 1-D quasi-steady analysis. CFD simulations have been performed by Tam and co-workers. In a series of papers[12,13,14], they studied slit and Helmholtz resonators using direct numerical simulation (DNS) techniques, first in a 2-D setup, and later in a 3-D configuration. The DNS approach is also pursued by Zhang and Bodony, who study the influence of laminar and turbulent grazing flow[6,15] and the interaction between neighboring cavity openings[16]. Mendez and Eldredge[17] determine the influence of purging flow via large eddy simulations (LES). The LES approach is also followed in the present study. Moreover, the linearized Navier-Stokes equations can be used to investigate the linear response of resonator as it is done by Tournadre et al.[18] for the investigation of temperature effects. An alternative approach to those solving explicitly the Navier-Stokes equations is the Lattice Boltzmann method, which is based on particle collision models and is promising low numerical cost, see for instance Ji and Zhao[19]. Another alternative is to characterize an orifice (corresponding to the resonator neck) by incompressible simulations and add the contribution of the compressible backing volume analytically[20].

On the side of the analytical modeling of Helmholtz resonators, a 1-D semi-empirical, quasi-steady approach is followed in the present study as often done in the literature. The idea of this ansatz is to analyze the Helmholtz resonator decomposed in an acoustically compact orifice and a compressible backing volume. The motion of the fluid in the neck can then be described by a 1-D quasi-steady equation containing semi-empirical correlations, see the studies by Ingard[21], Ingard and Ising[22], Melling[23], Cummings[24], Hersh et al.[25], as well as Singh and Rienstra[26].

Physically, resonators dissipate acoustic energy due to the thermo-viscous losses at the walls. It is well known that, for sufficiently high excitation amplitudes, additional acoustic energy is absorbed due to flow separation at the resonator edges. Flow separation processes are very sensitive to the edge shape. The edge shape impact has been investigated for open-end pipes by Disselhorst and Wijngaarden[27] as well as Atig et al.[28]. Temiz et al.[29] investigated this effect for orifice configurations. Its influence on the resonator impedance has been evaluated by Laudien et al.[30] and Förner et al.[31].

The acoustic dissipation by flow separation is a nonlinear phenomena. Its nonlinear behavior can be detected by two aspects for a harmonic excitation: On the one hand, amplitude and phase of the reflected wave at the frequency of excitation may depend on the amplitude of the excitation. This behavior can be described in terms of describing functions for the resonator impedance, or its reflection coefficient, see for instance Hersh et al.[25], Singh and Rienstra[26], or the Appendix of the present paper. On the other hand, scattering of acoustic energy to other frequencies may occur. To the authors' knowledge this has not yet been studied in detail for resonators. The scattering to higher harmonics at an orifice, which is closely related to the Helmholtz resonator, was studied experimentally and analytically

by Ingard and co-workers[22,32] as well as Cummings[24]. An "Odd-Harmonics-Only" (OHO) pattern in the higher harmonics was observed, where only the odd harmonics are present in the response. This observation could be explained by a quasi-steady analysis based on the Bernoulli equation.

The present study investigates the nonlinear acoustic scattering of both Helmholtz and quarter wave resonator designs by means of CFD simulations. The appearance of the OHO pattern is found to depend on the symmetry of the configuration under study. The quasi-steady theory for scattering to higher harmonics at symmetric orifices[24,32] is extended to also describe asymmetric configurations and flow conditions, such that it can be applied to Helmholtz resonators with an asymmetric neck or quarter wave resonators.

The paper is organized as follows: The approaches to describe the resonators response restricted to the fundamental frequency are presented in Sec. II. The quasi-steady theory from the literature is also introduced in this section. In Sec. III, this theory is applied for the considered cases and the scattering behavior is evaluated. Section IV presents the scattering behavior observed in the CFD simulations for both the Helmholtz and quarter wave resonators. The behavior is also compared to analytical prediction. Finally, the findings are summarized in Sec. V.

II.   Physical Background

In this section, the basic terminology to characterize acoustic resonators is introduced. Moreover, a quasi-steady analysis based on the incompressible Bernoulli equation is presented, which accounts for nonlinearities of the pressure drop across the neck of a resonator. Throughout the whole study, the geometrical quantities, shown in Fig. 1, are denoted as follows: For the Helmholtz resonators, the lengths and diameters of the neck and of the backing volume are referred to as l_0, d_0, l_{cav}, and d_{cav}, respectively. The length and diameter of the quarter wave resonator are named as l_0 and d_0. The open area ratio is denoted by σ.

II.A.   Impedance and Refection Coefficient Describing Functions

The behavior of an acoustic resonator is often described in the frequency domain by its *impedance* Z. It is defined as the ratio of the Fourier transforms ($\hat{\cdot}$) of the fluctuating acoustic pressure p' and velocity u' normal to the reference surface:

$$Z(\omega_0) = z(\omega)\, c_0 \rho_0 = \frac{\hat{p}(\omega_0)}{\hat{u}(\omega_0)} \ . \tag{1}$$

Here, ω_0 denotes the angular excitation frequency. The real part of the impedance is referred to as *resistance* and its imaginary part as *reactance*. In the following, impedance values
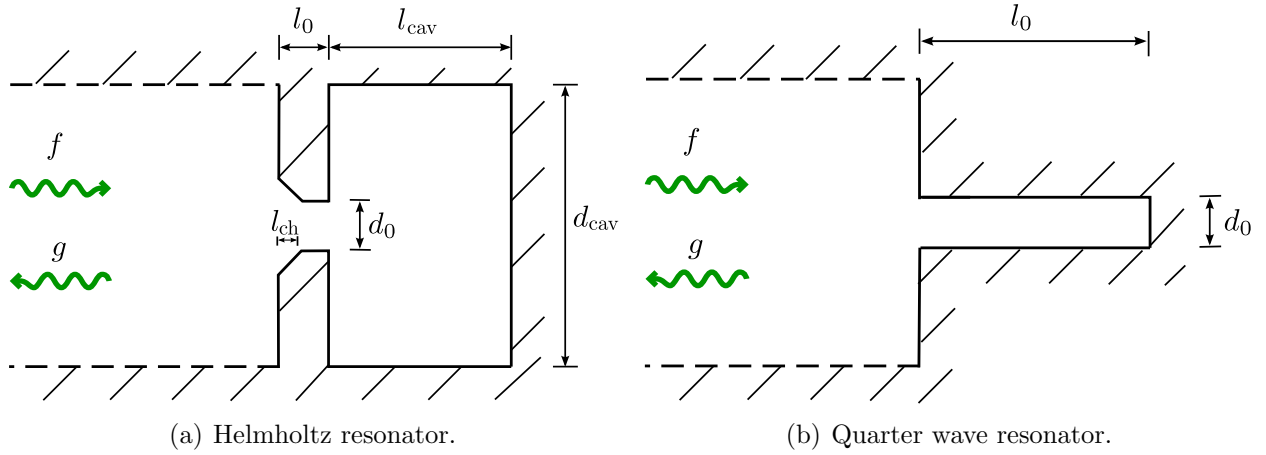
(a) Helmholtz resonator. (b) Quarter wave resonator.

Figure 1. Sketch of both resonator types considered. Slip walls in the simulations are marked by dashed lines.

normalized with the air specific impedance $\rho_0 c_0$ are denoted by lower case z. Here, ρ_0 and c_0 stand for the mean density and the speed of sound, respectively.

The resonator can also be characterized in terms of characteristic wave amplitudes f and g, assuming 1-D acoustics in front of the resonator. These f and g quantities can be considered as right and left traveling waves, respectively. In absence of mean flow, they are defined as $f = (p'/(\rho_0 c_0) + u')/2$ and $g = (p'/(\rho_0 c_0) - u')/2$. The ratio of the reflected $\hat{g}(\omega_0)$ wave to the normally incident $\hat{f}(\omega_0)$ wave in frequency domain is defined as the *reflection coefficient* $R(\omega_0) = \hat{g}(\omega_0)/\hat{f}(\omega_0)$. Its relation to the impedance is given by:

$$R(\omega_0) = \frac{\hat{g}(\omega_0)}{\hat{f}(\omega_0)} = \frac{Z(\omega_0) - \rho_0 c_0}{Z(\omega_0) + \rho_0 c_0} = \frac{z(\omega_0) - 1}{z(\omega_0) + 1} \ . \tag{2}$$

At the resonator angular eigenfrequency ω_{eig}, the reactance vanishes $\Im(Z(\omega_{\mathrm{eig}})) = 0$ and, accordingly, the optimal resistance equals the specific impedance $\rho_0 c_0$ of the medium, where no reflection takes place at all (i. e., $|R(\omega_{\mathrm{eig}})| = 0$). Thus, the gain of the reflection coefficient decreases with increasing SPL until it reaches the optimal resistance $\Re(z(\omega_{\mathrm{eig}})) = 1$. For a resistance larger than this optimal value $\Re(z(\omega_{\mathrm{eig}})) > 1$, the resonator is called *overdamped*. In that case, the reflection coefficient grows with a further increase of the resistance as can be also observed in Sec. IV.

The concepts introduced above are not adequate to characterize nonlinear phenomena since Z and R do not depend on the excitation amplitude. To extend the impedance to the nonlinear regime, the describing function approach is commonly used, see for instance Hersh *et al.*[25], which is referred to as *impedance describing function* in the following. Here, the impedance is specified not only in dependency on the frequency, but also on the excitation amplitude. This is commonly done in terms of the *sound pressure level* (SPL) present at a
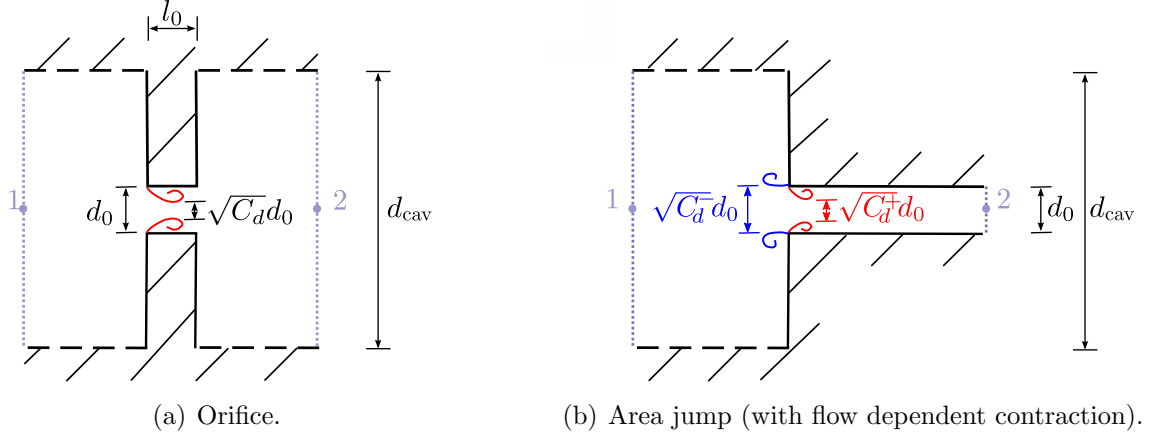
(a) Orifice.   (b) Area jump (with flow dependent contraction).

Figure 2. Sketch of the corresponding geometries for the incompressible quasi-steady analysis.

certain reference position. The value of this SPL is defined as $20 \log_{10}(p_{\mathrm{rms}}/p_{\mathrm{ref}})$, where p_{rms} and p_{ref} denote the root mean square of the fluctuating pressure and the reference pressure in air $20\,\mu\mathrm{Pa}$, respectively. Note that this approach cannot represent the nonlinear behavior in a comprehensive manner, but only the behavior for the fundamental frequency of excitation. In particular, the scattering to higher harmonics is not included in this describing approach, which is investigated in the current paper.

II.B. Flow Separation as the Cause of Nonlinear Behavior

The Helmholtz resonator can be analyzed as a combination of an acoustically compact orifice and a backing volume in the linear and nonlinear regime[20]. Thus, the loss mechanisms for a Helmholtz resonator are the same as those at an orifice. To understand those mechanisms, the 1-D unsteady Bernoulli equation with suitable extensions for the loss terms can be studied for an orifice as sketched in Fig. 2(a), see, e.g., references 32, 24 and 33. In the quarter wave resonator case, the situation is different due to the asymmetry of the area jump, as sketched in Fig. 2(b), but can be analyzed in a similar framework. The following discussion helps to understand how the nonlinear losses are caused in both configurations.

The analysis is presented in nondimensional form. Nondimensional quantities are indicated by $\tilde{\cdot}$. The reference time t_c, and pressure p_c used for the nondimensionalization are defined as:

$$t_c = \frac{l_c}{c_0} \quad \text{and} \quad p_c = \rho_0 c_0^2 \ . \tag{3}$$

The reference length scale l_c, which was already introduced above to define the time scale t_c, is set differently for the orifice and the area jump to account for the different typical scales present. It is set such that the corresponding nondimensional angular eigenfrequencies $\tilde{\omega}_{\mathrm{eig}} = \omega_{\mathrm{eig}}\, t_c$ for the Helmholtz and quarter wave resonators are unity, i.e., $\tilde{\omega}_{\mathrm{eig}} = \omega_{\mathrm{eig}}\, t_c = 1$.

These eigenfrequencies $\omega_{\text{eig}}^{\text{HR}}$ and $\omega_{\text{eig}}^{\text{QW}}$ for can be approximated as Helmholtz and quarter wave resonators

$$\omega_{\text{eig}}^{\text{HR}} = c_0 \sqrt{\frac{\sigma}{l_{\text{cav}} \left(l_0 + 2\,\Delta l\right)}} \quad \text{and} \quad \omega_{\text{eig}}^{\text{QW}} = \frac{\pi c_0}{2(l_0 + \Delta l)} \ , \tag{4}$$

respectively. The length correction Δl accounts for fluid in front of the resonator opening taking part in the oscillation and can be set according to Ingard[21] as $4/(3\,\pi)d_0$, where d_0 is the diameter of the opening. This geometrical length l_0 and the length corrections ($2\,\Delta l$ and Δl, respectively) are usually combined to the so-called effective lengths l_e, as described below in more detail in Eq. (7). The corresponding length scales are set as:

$$l_c^{\text{HR}} = \sqrt{\frac{l_{\text{cav}}\left(l_0 + 2\,\Delta l\right)}{\sigma}} \quad \text{and} \quad l_c^{\text{QW}} = \frac{2(l_0 + \Delta l)}{\pi} \ . \tag{5}$$

At first, the Helmholtz resonator is considered. It is assumed here that the resonator neck is acoustically compact such that it can be treated as an incompressible orifice. Viscous losses are neglected at the beginning of this consideration and the Bernoulli equation is studied. This equation reads in terms of fluctuating quantities in nondimensional form as:

$$\frac{\partial \tilde{\phi}'}{\partial \tilde{t}} + \frac{1}{2}\tilde{u}'^2 + \tilde{p}' = \text{const.} \ , \tag{6}$$

where $\tilde{\phi}$ is the nondimensionalized potential $\tilde{u} = \tilde{\nabla}\tilde{\phi}$. The equation above is integrated from position 1 to 2 sketched in Fig. 2(a). The nondimensionalized effective length $\tilde{l}_e$ is introduced to express the result in a compact form:

$$\tilde{\phi}'_2 - \tilde{\phi}'_1 = \int_1^2 \tilde{u}'(\tilde{x})\mathrm{d}\tilde{x} = \int_1^2 \frac{\tilde{A}_0 \tilde{u}'_0}{\tilde{A}(\tilde{x})}\mathrm{d}\tilde{x} = \tilde{u}'_0 \tilde{l}_e = \frac{\tilde{u}'}{\sigma}\tilde{l}_e \ . \tag{7}$$

Here, $\tilde{A}_0$ and $\tilde{u}'_0$ denote the nondimensionalized cross-section area and the velocity in the orifice, respectively. The $\tilde{x}$-dependent area formed by the flow path is $\tilde{A}(\tilde{x})$. Note that the effective length equals the nondimensionalized geometrical length of the orifice $\tilde{l}_0$ with an additional, nondimensionalized end correction $2\Delta\tilde{l}$ added, see, e.g., Ingard[21]. The pressure drop $\Delta\tilde{p}' = \tilde{p}'_1 - \tilde{p}'_2$ over the orifice without losses can be expressed as:

$$\Delta\tilde{p}' \approx \frac{1}{\sigma}\tilde{l}_e \frac{\partial \tilde{u}'}{\partial \tilde{t}} \ . \tag{8}$$

The losses caused by friction at the orifice walls, which are not considered in the above equation, can be included by an appropriate real valued constant $\tilde{R}_l$ (see, e.g., Bodén and Zhou[34]). When the acoustical partial displacement in the orifice reaches the same order as

the orifice diameter $\tilde{d}_0$ or is larger, i.e., when the *Strouhal number* $\mathrm{Sr} = \tilde{\omega}\,\tilde{d}_0\,\sigma/|\tilde{u}|$ is small, the flow cannot follow the edge contour anymore and separates. Thus, the flow takes less area to jet through the orifice as sketched in Fig. 2(a). The ratio of the flow core area to the geometrical cross-sectional area is described by the contraction factor C_d, which is also often referred to as discharge coefficient[15,25]. In the linear regime where $\mathrm{Sr} \gg 1$, it can be assumed $C_d \approx 1$, while $C_d < 1$ in the nonlinear regime. Besides the Strouhal number, also the edge shape has a strong impact on the separation process. The separation is more pronounced, the sharper the edge is[30,31]. Using the contraction factor, the velocity in the orifice can be expressed as $\tilde{u}_0' = 1/(C_d\,\sigma)\,\tilde{u}'$. When such a jet forms, it takes energy from the acoustics, which is dissipated in the vortex structures generated due to the separation. If it is assumed that the kinetic energy of the flow in the orifice $1/2\,(1/(C_d\sigma)\,\tilde{u}')^2$ is fully dissipated and does not recuperate downstream of the orifice (see for instance Ingard[32]), it follows

$$\Delta\tilde{p}' \approx \underbrace{\frac{1}{\sigma}\tilde{l}_e\frac{\partial\tilde{u}'}{\partial\tilde{t}}}_{\text{inertia}} + \underbrace{\tilde{R}_l\,\tilde{u}'}_{\text{viscosity}} + \underbrace{\frac{1}{2}\frac{\tilde{u}'\,|\tilde{u}'|}{(C_d\,\sigma)^2}}_{\text{flow separation}} \quad . \tag{9}$$

It can be seen in the expression above that the loss terms due to friction and flow separation contribute to the resistive part. When the losses and the pressure drop are not in equilibrium, the fluid in the orifice is accelerated, which impacts solely the reactance of the transfer impedance $(\widetilde{\partial\tilde{u}'/\partial\tilde{t}} = i\,\widetilde{\omega}\widetilde{u})$. Moreover, it can be seen that only the flow separation behaves in a nonlinear fashion in this model.

In analogy, an acoustically compact area jump, as sketched in Fig. 2(b), can be considered for the investigation of a quarter wave resonator. In comparison to the formulations for the orifice found in the literature, an additional term is introduced which also behaves nonlinearly. By integration of the Bernoulli equation (6), the additional term $1/2\,\tilde{u}'^2(1/\sigma^2 - 1)$ appears due the non-equal cross-section area on both sides. In this case, the pressure drop can be expressed as:

$$\Delta\tilde{p}' \approx \frac{1}{\sigma}\tilde{l}_e^{\,AJ}\frac{\partial\tilde{u}'}{\partial\tilde{t}} + \frac{1}{2}\,\tilde{u}'^2\left(\frac{1}{\sigma^2} - 1\right) + \tilde{R}_l^{AJ}\,\tilde{u}' + \frac{1}{2}\frac{\tilde{u}'\,|\tilde{u}'|}{(C_d\,\sigma)^2} \quad . \tag{10}$$

Above, $\tilde{l}_e^{\,AJ}$ and $\tilde{R}_l^{AJ}$ denote a suitable nondimensionalized effective length and linear loss term for the area jump, respectively.

III.   Scattering to Higher Harmonics Described by Quasi-Steady 1-D-Analysis

In contrast to linear systems, nonlinear systems can respond not only at the fundamental angular frequency ω_0 of the excitation, but also at its multiples, the so-called *higher harmonics*. The fundamental frequency ω_0 is referred to as the 1st harmonic, any multiples $n\,\omega_0$ as the nth harmonic ($n \in \mathbb{N}$). In the following, the spectrum of the response is studied numerically in dependency on the excitation frequency and amplitude. To the authors' knowledge, this is studied for the first time for resonator configurations in detail. The orifice, which is from a geometrical point of view close to the Helmholtz resonator, has been investigated with respect to its scattering behavior experimentally and analytically, see, e. g., Ingard and Ising[22,32] and Cummings[24]. A pattern in the harmonics has been observed in those studies, where the odd harmonics (3rd, 5th, ...) dominate clearly over the even ones (2nd, 4th, ...). This pattern is referred to as OHO ("Odd-Harmonics-Only") in the following. Ingard[32] and Cummings[24] explained the appearance of the OHO pattern by studying quasi-steady 1-D equations.

In the following, these considerations are extended step by step to account also for an asymmetric orifice and for an area jump as they are present for a Helmholtz resonator with asymmetric neck and a quarter wave resonator. This analysis is applied to predict the relative contributions of the first five harmonics for Helmholtz resonators with symmetric and asymmetric neck as well as quarter wave resonators.

The appearance or absence of the OHO pattern can be explained by studying quasi-steady 1-D equations as Eqs. (9) and (10). Similar considerations have been done by Ingard[32] and Cummings[24]. The theory presented in the literature is restricted to orifices assuming of a time-invariant contraction factor C_d for the whole cycle.

In the current study, the contraction coefficient C_d is assumed to be constant during the inflow and outflow half-cycle:

$$C_d = \begin{cases} C_d^+, & \text{for } \tilde{u}' \geq 0 \\ C_d^-, & \text{for } \tilde{u}' < 0 \end{cases} . \tag{11}$$

First, the orifice is considered where the pressure drop is described by Eq. (9). The only nonlinear term is given as $1/[2(C_d\,\sigma)^2]\,\tilde{u}'\,|\tilde{u}'|$. Accordingly, this is the only term that can contribute to the scattering to higher harmonics. Thus, the other terms are disregarded in the analysis since the focus of the study is the scattering behavior to higher harmonics, i. e.,

$$\Delta \tilde{p}'(\tilde{t})\,2\sigma^2 = \frac{1}{C_d^2}\,\tilde{u}'\,|\tilde{u}'| \ . \tag{12}$$

If a sinusoidal velocity $\tilde{u}'(\tilde{t}) = \tilde{A}_u \sin(\tilde{\omega}_0\tilde{t})$ is assumed, the Fourier series of this pressure drop reads as

$$\Delta\tilde{p}'(\tilde{t})\frac{2\sigma^2}{\tilde{A}_u^2} = \frac{a_0}{2} + \sum_{n=1}^{\infty} a_n\cos(n\tilde{\omega}_0\tilde{t}) + b_n\sin(n\tilde{\omega}_0\tilde{t}) \tag{13}$$

with the constants

$$a_n = \begin{cases} \frac{1}{2}(C_d^+ - C_d^-), & \text{for } n = 0 \\ \frac{1}{4}(C_d^- - C_d^+), & \text{for } n = 2 \\ 0, & \text{else} \end{cases} \tag{14}$$

and

$$b_n = \begin{cases} \frac{-4(C_d^- + C_d^+)}{\pi(n^3 - 4n)}, & \text{for odd } n \\ 0, & \text{else} \end{cases} \tag{15}$$

It can be seen that, for symmetric flow conditions with $C_d^+ = C_d^-$, the coefficients $a_n = 0$ for all n. Thus, only contributions with $b_n \neq 0$ remain for odd n. It can be concluded that the appearance of the OHO pattern is due to the symmetry of the flow.

This flow symmetry is broken for an asymmetric geometry. Note that also mean flow may lead to different flow contraction condition during the inflow and outflow phase, as shown by Zhang and Bodony[35] for a Helmholtz resonator with grazing flow. The flow asymmetry due to flow separation at sufficient high amplitudes can be described like this for an one-sided chamfered orifice: At the sharp orifice edge, the flow contracts, i.e., $C_d^+ < 1$, while it does not at the chamfered edge, i.e., $C_d^- \approx 1$.

The asymmetry increases when the area jump is studied instead of the orifice. The separation term (Eq. (12)) analyzed by Fourier transformed in Eqs. (13)– (15) is also part of the nonlinear response. Due to the change in cross-section at the area jump, an additional term appears in Eq. (10). This term can be expressed as:

$$\frac{1}{2}\tilde{A}_u^2\sin^2(\tilde{\omega}_0\tilde{t})\left(\frac{1}{\sigma^2} - 1\right) = \frac{1}{4}\tilde{A}_u^2\left(\frac{1}{\sigma^2} - 1\right)\left(1 - \sin(2\tilde{\omega}_0\tilde{t})\right) \ . \tag{16}$$

The expression above contributes significantly to the 2$^{\text{nd}}$ harmonic and, thus, amplifies the disappearance of the OHO pattern.

The following conclusions can be made from the considerations above: The Helmholtz resonator with symmetric neck shows the OHO pattern, where the harmonics decrease with increasing order. If its neck is asymmetric (e.g., with $C_d^+ \approx 0.7$ for sharp edged and $C_d^- \approx$ 0.95 for 45° chamfered edge, see reference 36), the OHO pattern gets weaker. The 3$^{\text{rd}}$ harmonic is still dominant. But now the 2$^{\text{nd}}$ harmonic is predicted to be more pronounced than the 5$^{\text{th}}$ one. When a quarter wave resonator is considered, strong scattering in the 2$^{\text{nd}}$ harmonic is expected. Overall, the scattering to higher harmonics is here much larger than

Table 1. Geometric properties of the considered Helmholtz and quarter wave resonators in dimensional and nondimensional form.

	l_0 [mm]	d_0 [mm]	l_{cav} [mm]	d_{cav} [mm]	l_{ch} [mm]	σ [%]	$\omega_{\text{eig}}/(2\pi)$ [Hz]
HRS	4.0	4.2	20	50	0	0.71	373
HRA	4.0	4.2	20	50	0.35	0.71	373
QW	143	6.35	–	–	–	1.56	589
	$\tilde{l}_0$ [-]	$\tilde{d}_0$ [-]	$\tilde{l}_{\text{cav}}$ [-]	$\tilde{d}_{\text{cav}}$ [-]	$\tilde{l}_{\text{ch}}$ [-]	σ [%]	$\tilde{\omega}_{\text{eig}}$ [-]
HRS	0.0274	0.0288	0.1369	0.3423	0	0.71	1
HRA	0.0274	0.0288	0.1369	0.3423	0.0024	0.71	1
QW	1.5561	0.0691	–	–	–	1.56	1

in the case of a Helmholtz resonator (for $\sigma \ll 1$).

In the discussion above, only the nonlinear terms are considered. It can be seen in Eqs. (13) and (16) that their contribution scales with the square of the amplitude of the velocity $\tilde{A}_u^2$, while all the other linear terms scale with the amplitude of the velocity $\tilde{A}_u$. Thus, it can be concluded that the impact of the nonlinear term responsible for the scattering to higher harmonics rises with increasing velocity.

IV.   Scattering to Higher Harmonics Observed in CFD Simulations

In this section, the predicted patterns in the amplitudes of the higher harmonics are verified and quantified with compressible CFD simulations for three resonator configurations. These considered configurations as well as the computational setup are introduced in Sec. IV.A. A qualitative comparison of compressible Helmholtz resonator simulations and incompressible orifice simulations is performed in Sec. IV.B. By doing so, a link from the incompressible theory to compressible resonator simulations is provided. Moreover, the flow separation for the three test cases is investigated during the inflow and outflow phase in this section. Finally, the results of the compressible simulations of three resonators are presented and discussed in Sec. IV.C.

IV.A.   Simulation Setup and Definition of the Test Cases

IV.A.1.   Definition of Test Cases

In the present numerical study, a quarter wave resonator (QW) as well as Helmholtz resonators with symmetric (HRS) and asymmetric neck (HRA) are considered. The generic geometries are sketched in Fig. 1. The neck of configuration HRA is chamfered by 45° on

the outside with a length in axial direction of $l_{\mathrm{ch}} = 0.35\,\mathrm{mm}$. The values of all geometric quantities are listed in Tab. 1 in dimensional and nondimensional form. The configuration HRS is set as in reference 31 to have access to validation data. The chamfer length is set small enough that it influences the linear response of the resonator only marginally.

IV.A.2. CFD Solver Setup

Compressible CFD simulations are performed with the PIMPLE algorithm of OpenFOAM[37]. The slip condition is applied at the cylindrical wall of the impedance tube and the no-slip condition is used at the resonator itself, see Fig. 1. At the inlet, the *Navier-Stokes characteristics boundary condition* (NSCBC), cf. Poinsot and Lele[38], is utilized. This boundary condition ensures a low acoustic reflection of the outgoing g wave. Simultaneously, an excitation signal can be imposed for the incoming f wave, which set sinusoidally $f = A_f \sin(\omega_0 t)$ with different fundamental frequencies $\omega_0/(2\pi)$. At this inlet plane, the fluctuating pressure p' and velocity u' are monitored. From these dimensional quantities, the time series of the nondimensional $\tilde{f}$ and $\tilde{g}$ waves can be computed directly. As explained above, the incoming wave scatters in the harmonics of the reflected wave $\widehat{\tilde{g}}(n\,\tilde{\omega}_0)$. In the following figures, the amplitudes of the higher harmonics $\widehat{\tilde{g}}(n\,\tilde{\omega}_0)$ are normalized by the amplitude of the fundamental harmonic of the incoming wave $\widehat{\tilde{f}}(\tilde{\omega}_0)$, which can be written as:

$$\frac{\left|\widehat{\tilde{g}}(n\,\tilde{\omega}_0)\right|}{\left|\widehat{\tilde{f}}(\tilde{\omega}_0)\right|}. \tag{17}$$

In the post-processing, the transient parts of the data series have been removed and then truncated to a multiple of the period T to avoid leakage in the spectra. For further details on the solver refer to reference 31. The simulations use 3-D meshes of at least 1.5 million cells. Note that this is overall a rather coarse mesh in comparison to DNS simulations available in the literature[15]. However, the mesh is refined carefully in the Helmholtz resonator neck (and the quarter wave resonator mouth, receptively) and, especially at the edges, since here the mechanisms responsible for the acoustic dissipation take place. The mesh independence with respect to the acoustic impedance has been checked for HRS up to a overall SPL of $125\,\mathrm{dB}$. Overall, reasonable results with relatively low computation cost can be achieved enabling for extensive parameter studies.

The compressible CFD simulations are performed as LES with the k-equation eddy-viscosity model as subgrid scale (SGS) model. Several SGS models have been tested. However, the acoustic response of the resonator depends only very weakly on the SGS modeling. Vortex structures are formed in the vicinity of the resonator neck due to the pulsation forcing of the flow. The dissipation to thermal energy of these vortices follows mainly the turbulent

cascade. However, the separation process itself, responsible for the nonlinear acoustic dissipation, is almost not influenced by the vortices. This can also be seen with the Reynolds number based on the orifice size and velocity amplitude at the orifice, which remains rather low (maximum Re≈ 3000 at 119.7 dB for HRS). Accordingly, the impact of the SGS model on acoustic properties remains very small as the separation process at the edges is resolved sufficiently. Moreover, comprehensive parameter studies regarding mesh, time-step, and solver parameters have been performed to ensure that the presented results are independent of the numerical settings. The solver has been validated in detail in the linear regime for various configurations in reference 31. In the nonlinear regime, the solver is validated against measurements of M. A. Temiz[39] based on a describing functions for configuration HRS, see Appendix.

To compare the simulation with measurement, the input amplitude A_f of the f waves must be set such that the superposition of the waves f and the reflected $g = Rf$ matches the desired SPL, see reference 20 for more details. This requires an a priori knowledge of the reflection coefficient or an iterative process. In the following, this approach of setting the input amplitude is solely used for validation purposes. Besides that, the SPL is set only with respect to the input signal f ignoring the reflected acoustic g wave. This is referred to as *input SPL* in the following. Note that the input SPL and the actual SPL differ from each other.

For the orifice configuration, also incompressible simulations are performed with the SIMPLE algorithm of the commercial software ANSYS Fluent v15. A detailed description of the corresponding solver setting can be found in reference 20. For a given geometry and excitation frequency, the nonlinear behavior is linked to the magnitude of the velocity in the orifice and resonator neck, respectively. For a valid comparison, the input amplitude in the incompressible simulation has to be set such that velocities in the orifice agree with the velocities in the Helmholtz resonator neck.

IV.B. Validation of Modeling Assumptions via CFD

IV.B.1. *Linking the Incompressible and Compressible Approaches*

The orifice is treated incompressible in the analysis of Sec. III, while the CFD simulations of the Helmholtz resonator are set up compressibly. Accordingly, a quantitative comparison between those two is not directly possible. Therefore, also incompressible orifice CFD simulations are considered in this section, which allows a link from the CFD simulations to the 1-D quasi-steady theory. The compressible resonator simulations and the incompressible orifice simulations can be compared qualitatively.

A sinusoidal velocity $\tilde{u}'(\tilde{t}) = \tilde{A}_u \sin(\tilde{\omega}_0 \tilde{t})$ is assumed in the analysis of Sec. III. The
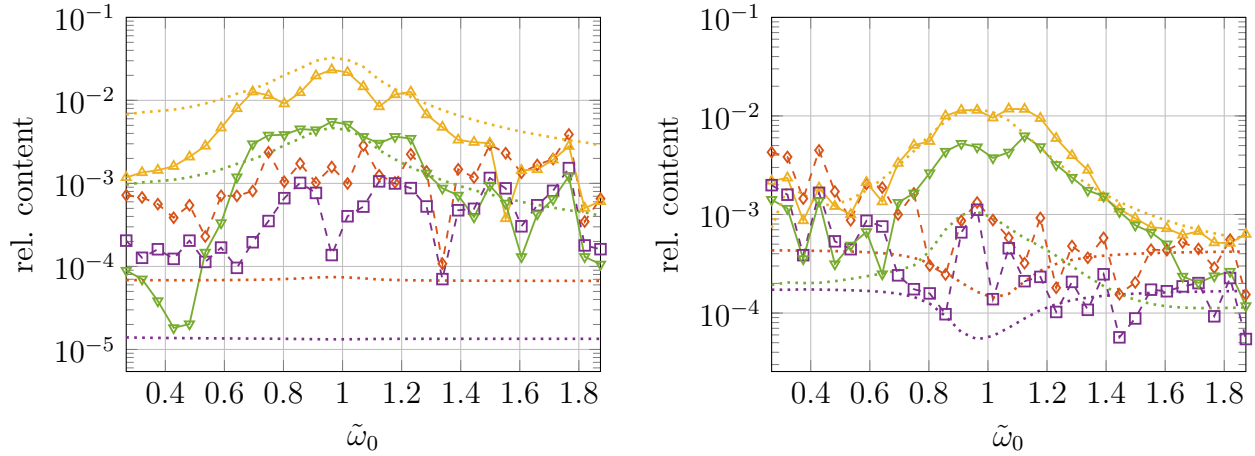
(a) Higher harmonics in $\Delta p'$ at the orifice (cf. Eq. (18)). (b) Higher harmonics in f for the Helmholtz resonator (cf. Eq. (17)).

Figure 3. Higher harmonics for the Helmholtz resonator HRS and the corresponding orifice with an excitation corresponding to a SPL of $119.7\,$dB: **2$^{\text{nd}}$ harmonic in CFD simulations** - ◇ -, **3$^{\text{rd}}$** —△—, **4$^{\text{th}}$** - ◻ -, **5$^{\text{th}}$** —▽—; **2$^{\text{nd}}$ harmonic with quasi-steady 1-D analysis** ⋯⋯, **3$^{\text{rd}}$** ⋯⋯, **4$^{\text{th}}$** ⋯⋯, **5$^{\text{th}}$** ⋯⋯.

higher harmonics occur there solely in the pressure drop $\Delta\widehat{\widetilde{p}}(n\,\tilde{\omega}_0)$ over the orifice. This pressure drop including the higher harmonics is also determined via incompressible CFD simulations with sinusoidal velocity excitation. For these incompressible simulations, the orifice corresponding to the resonator neck of HRS is considered as geometry. The amplitudes A_u of the velocities in the incompressible simulations are adjusted such that they coincide with the velocity amplitudes in the resonator neck present for a SPL of $119.7\,$dB at the reference distance $l_{\text{ref}} = 49.7\,$mm. The higher harmonics in the pressure drop are presented in Fig. 3(a). In this figure, the amplitude of the nth harmonic is normalized by the fundamental harmonic $\Delta\widehat{\widetilde{p}}(\tilde{\omega}_0)$, such that this harmonic is represented as

$$\frac{\left|\Delta\widehat{\widetilde{p}}(n\,\tilde{\omega}_0)\right|}{\left|\Delta\widehat{\widetilde{p}}(\tilde{\omega}_0)\right|} \,. \tag{18}$$

Moreover, the results of 1-D simulations[40] of the quasi-steady equation (9) are included in this figure. It can be observed that both the 1-D quasi-steady equation (9) and the incompressible CFD simulation exhibit the OHO predicted by the quasi-steady analysis. The 3$^{\text{rd}}$ harmonic is dominant followed by the 5$^{\text{th}}$ harmonics, as predicted by the analysis. The magnitude of the odd harmonics obtained by the 1-D simulations of the quasi-steady equation (9) agrees well with the one of the CFD simulations. The scattering to higher harmonics takes place mainly close to the angular eigenfrequency $\tilde{\omega}_{\text{eig}} \approx 1$, where the velocities in the orifice are largest.

In Fig. 3(b), the higher harmonics in the scattered g wave (as defined in Eq. (17)) are plotted for the compressible LES simulations of the symmetric Helmholtz resonator. Again, the input amplitudes A_f are set in a way that a SPL of 119.7 dB at the reference distance $l_{\text{ref}} = 49.7$ mm is achieved. The 1-D quasi-steady equation (9) can be rewritten in terms of Riemann invariants f and g to a 1-D ordinary differential equation (ODE), which can be solved numerically[40]. The scattered higher harmonics described by this 1-D quasi-steady ODE are also included in this figure. Both compressible approaches, the LES and the 1-D ODE, have the OHO pattern as predicted by the 1-D quasi-steady analysis in Sec. III. There are almost no contributions to the even harmonics for both compressible approaches. Also here, the scattering to higher harmonics occurs mainly close to the angular eigenfrequency, $\tilde{\omega}_0 \approx 1$. This also agrees with the incompressible analysis, since the velocities in the resonator neck are largest close to the eigenfrequency. It can be observed that the 3$^{\text{rd}}$ harmonics of this quasi-steady 1-D approach agree very well these of the 3-D LES simulations. The 5$^{\text{th}}$ harmonic is under-predicted by the 1-D approach. Overall, the nonlinear term in the quasi-steady equation (9), once written in terms of Riemann invariants, describes the mechanisms responsible for the scattering to higher harmonics accurately.

It can be summarized that the OHO pattern is present for both symmetric orifices and Helmholtz resonators. For both configurations, the mechanism responsible for the scattering to higher harmonics can be explained well by studying the 1-D quasi-steady equation (9) as it is done in Sec. III.

IV.B.2. Contraction Behavior for the Three Considered Configurations

Before the scattering to higher harmonics in the compressible CFD simulations for each resonator is discussed, the flow contraction is investigated for these configurations. In Fig. 4, a snapshot of the flow field during the inflow and outflow phase with maximal contraction is presented for all configurations. These snapshots are cropped to the vicinity of the resonator neck and mouth, respectively. Note that the separation process is a transient process such that for a precise prediction phase averaging over several periods and, subsequently, averaging over time would be required as it is done by Zhang and Bodony[15]. Here, only the order of magnitude and the influence of the edge on separation behavior is evaluated optically with the presented snapshots. The separation zones are marked in green at the upper edges in each figure. The resonators are excited at a frequency close their eigenfrequencies $\tilde{\omega}_0 \approx 1$ (corresponding to 380 Hz) with an input SPL of 125 dB (for HRS and HRA) and at $\tilde{\omega}_0 \approx 1$ (corresponding to 580 Hz) with 160 dB (for QW). Configuration QW is excited with a higher SPL in comparison to the Helmholtz resonator configurations since it requires a higher SPL to trigger nonlinear behavior as it shown below in Sec. IV.C.3. As explained above, these SPL values are set here and in the following as input SPLs, which means that
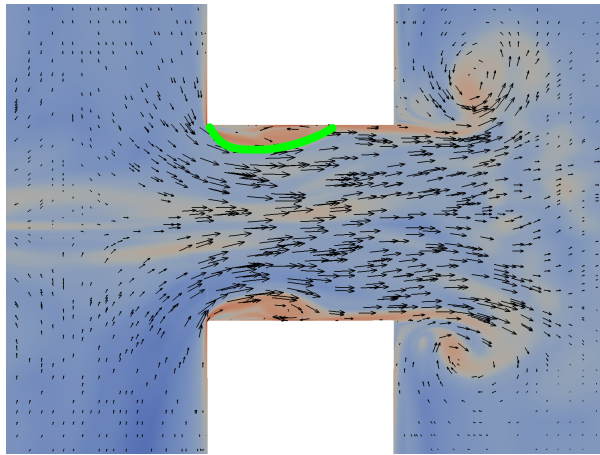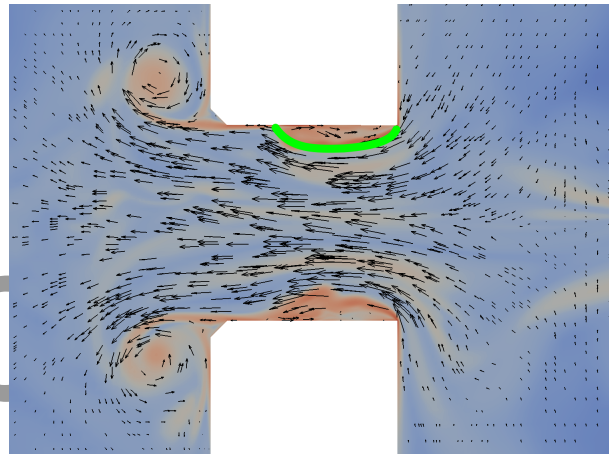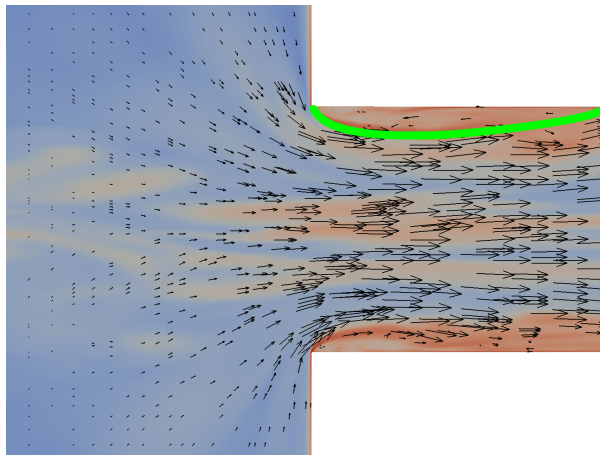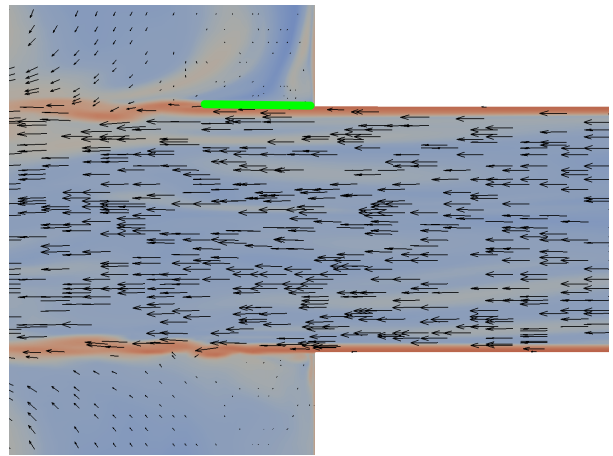
(a) HRS inflow.
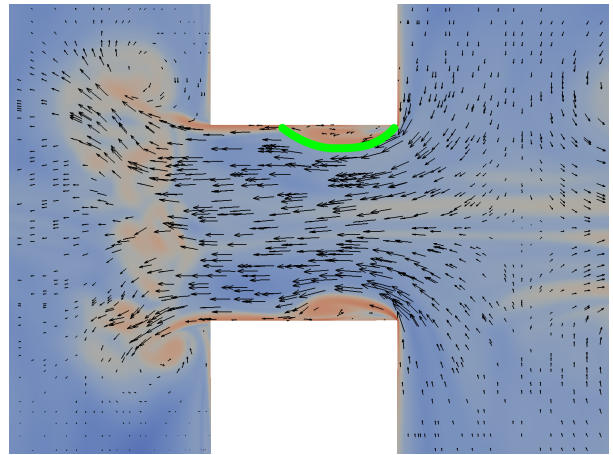
(b) HRS outflow.
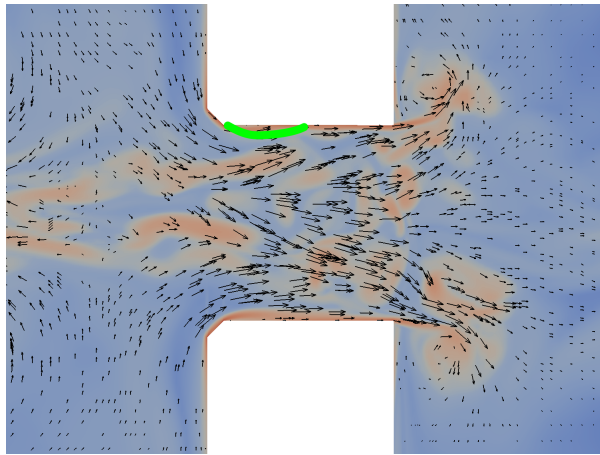
(c) HRA inflow.

(d) HRA outflow.

(e) QW inflow.

(f) QW outflow.

Figure 4. Flow visualization in a 2-D cutting plane in the vicinity of the resonator neck/mouth during the inflow and outflow phases for the three configurations considered at excitation frequency close to the eigenfrequency $\tilde{\omega}_0 = 1$ with input SPL $125\,\text{dB}$ for HRS and HRA, and with input SPL $160\,\text{dB}$ for QW. On the upper half, the contraction is marked in green for each case.

the SPL values refer solely to the input f waves while ignoring the reflected g waves. The separation behavior is similar for the inflow and outflow for HRS, see Figs. 4(a) and 4(b). A contraction ratio of ≈ 0.7, as can be found in the literature[15,36], is confirmed by the simulation. The asymmetric neck induces an asymmetric separation behavior. During the outflow, the contraction remains the same as for HRS, see Fig. 4(d). However, the flow contracts less with a factor $C_d^+ \approx 0.9$ for the inflow (Fig. 4(c)), which is close to literature values (0.95 in Blevins' textbook[36]). The separation is also asymmetric for the quarter wave resonator QW with $C_d^+ \approx 0.7$ and $C_d^- \approx 1$ as can be seen in Figs. 4(e) and 4(f). Overall, it can be concluded that the assumption of Sec. III that the contraction depends on the flow direction is reasonable.

IV.C.   Scattering to Higher Harmonics Determined by CFD Simulations

IV.C.1.   Scattering to Higher Harmonics at the Helmholtz Resonator with Symmetric Neck

The amplitudes of the higher harmonics $n\tilde{\omega}_0$ up to order $n = 5$ of the resonator response for an input SPL of 125 dB are plotted in Fig. 5(a) for the fundamental excitation frequency $\omega_0/(2\pi)$ in the range of [200 - 700] Hz corresponding to $\tilde{\omega}_0 \in [0.54, 1.87]$. All harmonics with larger order ($n > 5$) are negligible with a relative content of $< 2\,\text{‰}$. It can be observed that the damping of the fundamental harmonic (——) is best close to the resonator eigenfrequency, i. e., where $\tilde{\omega}_0$ is close to unity. On the other hand, scattering to higher harmonics mainly occurs close to that frequency. This is in line with expectations since the velocity in the neck is largest in this frequency range and is causing strong nonlinear effects here. Away from the eigenfrequency, velocities are smaller and the system behaves almost linearly. As expected, the OHO pattern occurs, i. e., the odd harmonics contribute predominantly to the response, while the even harmonics are almost absent. The 3rd harmonic (——) clearly dominates over the even ones (2nd (- ◆ -) , 4th (- ☐ -) , . . .). The contribution of the harmonics becomes less and less considerable with increasing order n. The impact of the 5th harmonic (——) is noticeably smaller than the 3rd but is still more prominent than even harmonics.

In Fig. 5(b), the scattering to the harmonics is depicted under variation of the input SPL for an excitation frequency close to eigenfrequency $\tilde{\omega}_0 \approx 1$ (corresponding to $\omega_0/(2\pi) = 380\,\text{Hz}$). The reflection coefficient and the resistance are presented in Fig. 6 (——). Note that the reflection coefficient equals the scattering into the fundamental harmonic, which is also shown in Figs. 5(a) and 5(b). With increasing input SPL, the fundamental harmonic first decays (up to 110 dB), since the resistance increases, see Fig. 6(b). The optimal damping for orthogonal incident acoustic waves is achieved with a normalized impedance $z = 1$. Increasing the excitation further leads to higher resistance, but also the reflection increases. This occurs due to the over-damping of the system. The trend of increasing resistance with
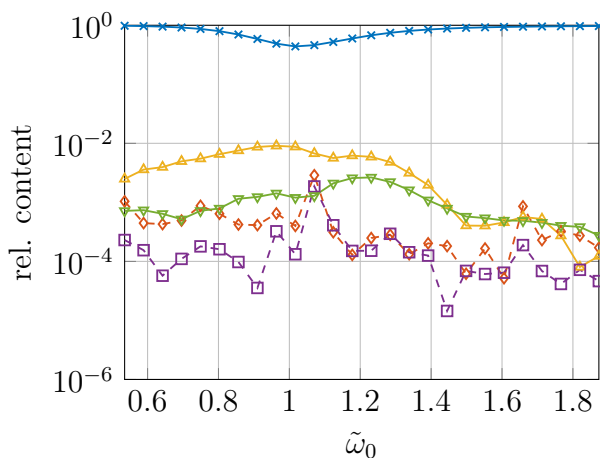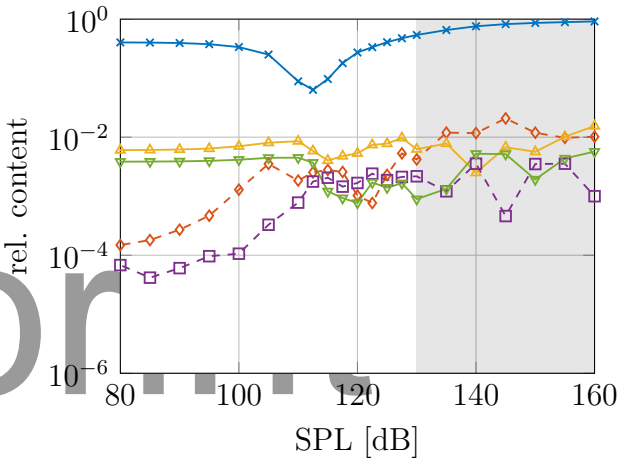
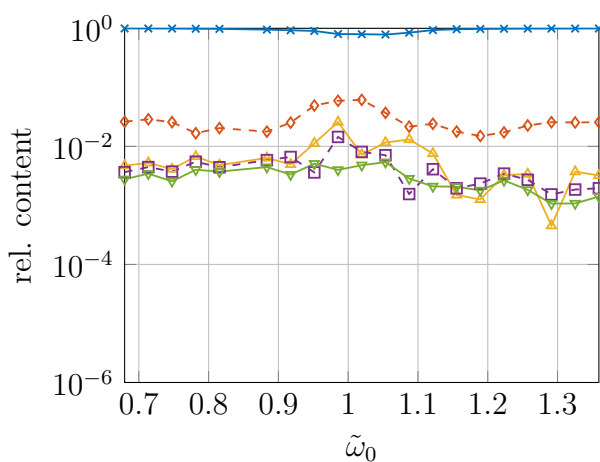(a) Helmholtz resonator HRS for input SPL 125 dB.
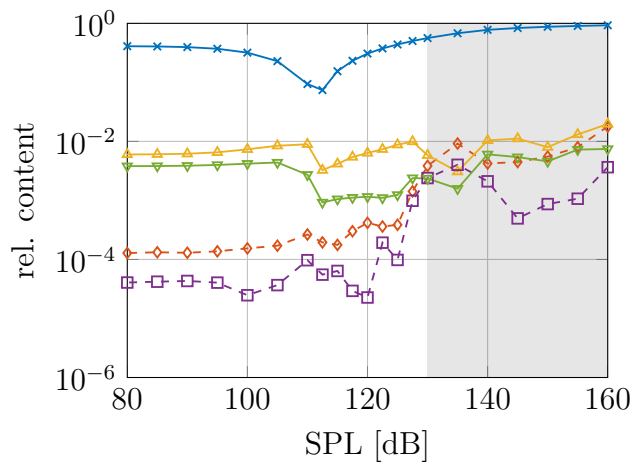
(b) Helmholtz resonator HRS at $\tilde{\omega}_0 \approx 1$ (380 Hz) for variable input SPL.
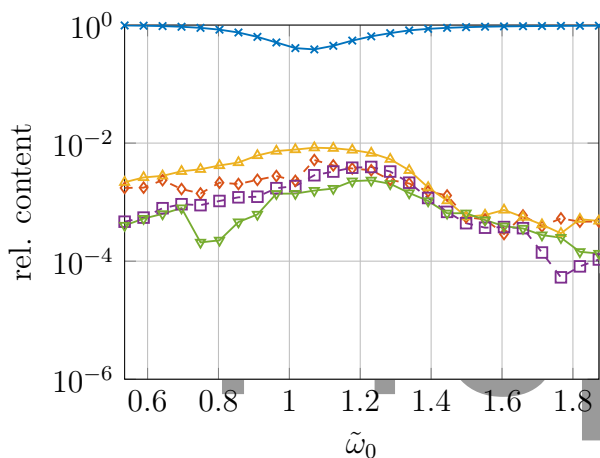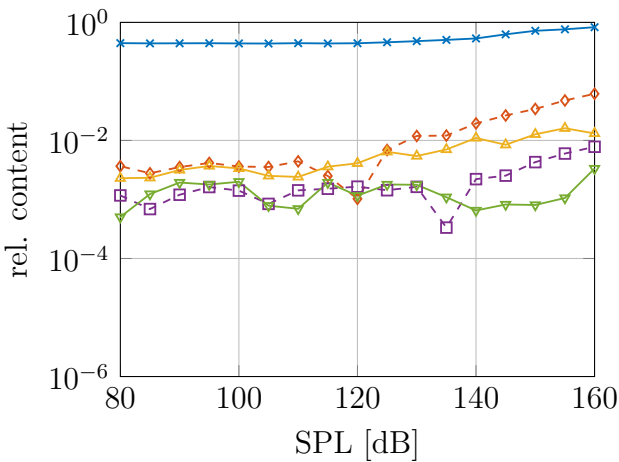
(c) Helmholtz resonator with asymmetric neck HRA for input SPL 125 dB.

(d) Helmholtz resonator with asymmetric neck HRA at $\tilde{\omega}_0 \approx 1$ (380 Hz) for variable input SPL.

(e) Quarter wave resonator QW for input SPL 160 dB.

(f) Quarter wave resonator QW at $\tilde{\omega}_0 \approx 1$ (580 Hz) for variable input SPL.

Figure 5. **Scattering to harmonics plotted in logarithmic scale for the three considered test cases: 1st, fundamental** ——×—— ; **2nd** – –◇– – ; **3rd** ——△—— ; **4th** – –□– – ; **5th** ——▽—— .

(a) Normalized resistance $\Re(z)$.
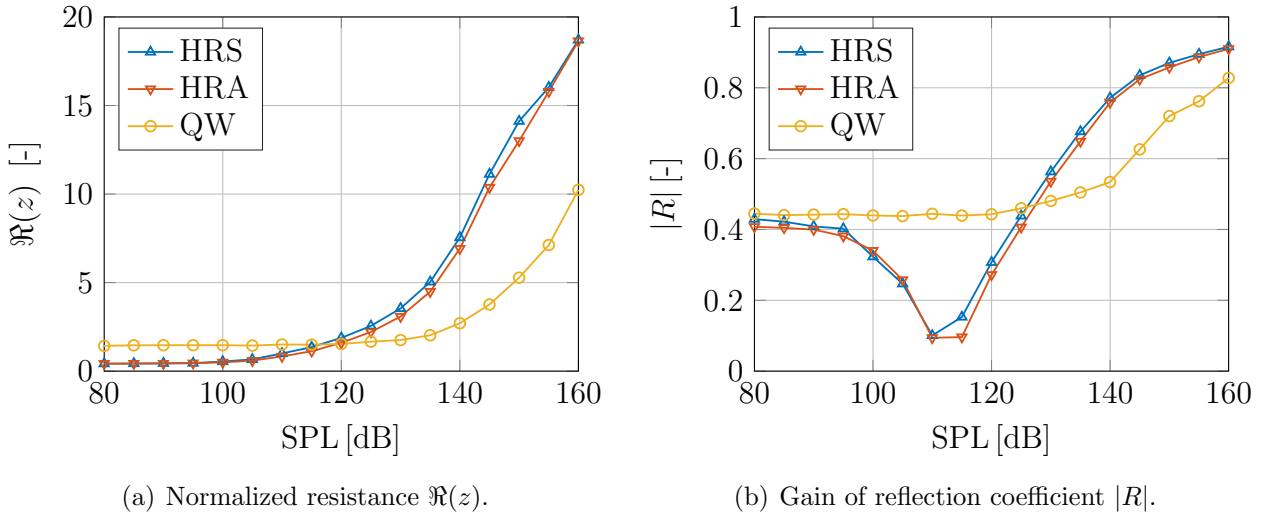
(b) Gain of reflection coefficient $|R|$.

Figure 6. Gain of reflection coefficient $|R|$ and normalized resistance $\Re(z)$ under variation of the input SPL at the corresponding eigenfrequency $\tilde{\omega}_0 \approx 1$ ($\omega_0/(2\pi) = 380\,\mathrm{Hz}$ and $\omega_0/(2\pi) = 580\,\mathrm{Hz}$, respectively) for the three configurations considered.

increasing SPL can also be explained by studying the 1-D equation for the pressure drop, see Eq. (9). The only nonlinear term in this equation corresponds to the flow separation. The corresponding nonlinear resistance scales with the amplitude of the velocity in the neck, which itself increases with rising SPL. This can also be seen in experimental[41] and numerical[15] studies.

The scattering to higher harmonics increases with increasing amplitude in the normal-damped range ($z < 1$). Close to the region of optimal damping ($z = 1$), the scattering to higher harmonics attains abruptly a local minimum. This minimum cannot be explained with the analysis of Sec. III, since the velocity in the neck is actually further increasing. Furthermore, the scattering to higher harmonics does not totally vanish for low amplitudes. The considerations made above would actually suggest a monotonic increase of the scattering with the amplitude, starting with no scattering and reaching asymptotically a limit. The reasons for the discrepancy to the presented simulation results are still unknown. In the over-damped range, the scattering increases again by increasing the input SPL. The overall scattering remains small for this resonator setup even for very high excitation levels. Thus, modeling the nonlinear behavior only for the fundamental frequency $\tilde{\omega}_0$ with the describing function approach (see Sec. II.A) reflects the main mechanisms accurately in that case.

It can be observed that the OHO pattern vanishes in a range of very high SPL ($\geq 130\,\mathrm{dB}$), which is shaded in gray in Figs. 5(b) and 5(d) (for HRA). The interaction of the vortices formed at leading and trailing edges was identified as the cause of this behavior. The exact mechanism and the circumstances when the OHO pattern is absent will be discussed in detail in a separate article.

IV.C.2. Scattering to Higher Harmonics at the Helmholtz Resonator with Asymmetric Neck

The gain of the reflection coefficient and resistance for various SPLs are included in Fig. 6 for the configuration with the asymmetric neck HRA. The chamfer size has been set such that the linear impedance is almost not influenced by the chamfer. Thus, the eigenfrequency remains the same as for HRS and the excitation for that case is also set to 380 Hz. The nonlinear resistance can be observed to decrease slightly in comparison to the unchamfered case HRS, see Fig. 6(a). This decrease arises from the lower flow contraction during the outflow phase, see reference 31. The scattering to the harmonics $n\tilde{\omega}_0$ ($n \in \{1, 2, \ldots, 5\}$) is shown for an input SPL of 125 dB in Fig. 5(c) for a range of $[200 - 700]$ Hz for the fundamental excitation frequency $\omega_0/(2\pi)$, corresponding to $\tilde{\omega}_0 \in [0.68, 1.36]$. Moreover, the scattered higher harmonics are presented for an excitation close to eigenfrequency $\tilde{\omega}_0 \approx 1$ (corresponding to 380 Hz) with varying input SPL in Fig. 5(d). As predicted, the 2nd harmonic increases in comparison to HRS with symmetric neck. According to the analysis of Sec. III, the 2nd harmonic should be weaker than the 3rd but stronger than the 5th one. However, the increase of the 2nd harmonic is moderate such that the 2nd and 5th harmonics have about an equal strength in the CFD simulations.

IV.C.3. Scattering to Higher Harmonics at the Quarter Wave Resonator

For the quarter wave resonator, the behavior changes significantly with respect to the Helmholtz resonators. For QW, the scattering to higher harmonics is mostly into the 2nd harmonic, which again fits well to the analysis of Sec. III. This can be seen in Fig. 5(e) for a constant SPL of 160 dB and in Fig. 5(f) for the excitation eigenfrequency close to eigenfrequency $\tilde{\omega}_0 \approx 1$ (corresponding to 580 Hz) in a range of $[80 - 160]$ dB. The frequency sweep is performed for QW at 160 dB instead of 125 dB for Helmholtz resonator configurations due to the higher SPL required to trigger nonlinear behavior. This can be seen in Fig. 6(a) (—⊸—). For HRS, the resistance starts to increase at a SPL of about 105 dB due to nonlinear effects. For QW, this occurs at about 125 dB. This difference can be explained only partially due to the different open area ratios σ. Thus, the different threshold to trigger nonlinearities originates mainly due to the different resonator concepts. Moreover, the overall scattering increased as well. The maximal scattering was in the order of 2 % for the Helmholtz resonators. Here for QW, the relative scattering to the 2nd harmonic can reach values up to the order of 10 %. This difference in magnitude of the Helmholtz and the quarter wave resonator is backed by the quasi-steady analysis.

V.   Summary and Conclusion

The nonlinear acoustic response of quarter wave and Helmholtz resonators has been studied by means of compressible CFD simulations. Particular attention was paid to the scattering to higher harmonics. For the Helmholtz resonators the higher harmonics exhibit an odd-harmonics-only (OHO) pattern, where only the odd harmonics are present, while the even ones are negligible. Such patterns were observed previously at symmetric orifices, and explained by a 1-D quasi-steady analysis based on the Bernoulli equation with suitable extra terms for the losses[22,24,32]. The current study extends the analysis, such that it is applicable also to configurations that exhibit asymmetric flow patterns, e.g. Helmholtz resonators with an asymmetric necks, or quarter wave resonators.

The following observations are observed in CFD simulations and confirmed by the quasi-steady analysis: For the Helmholtz resonator with a symmetric neck, the scattering to higher harmonics exhibits the OHO pattern. The OHO pattern is weaker if a Helmholtz resonator with an asymmetric neck is considered. It is concluded that the pure OHO pattern occurs due to the flow symmetry during the inflow and outflow phase through the symmetric resonator neck. For the quarter wave resonator – corresponding to a simple discontinuity in cross-sectional area in the 1-D compact analysis – a larger threshold for the excitation is required to trigger noticeable nonlinear effects. If scattering takes place in this configuration, the 2nd harmonic is the dominant higher harmonic, and the OHO pattern vanishes completely.

Overall, the scattering to higher harmonics is more pronounced for the quarter wave resonator, for which values up to the order of 10% of the incident wave are observed. In contrast, Helmholtz resonators exhibit quite moderate nonlinear scattering (up to 2%) even for very high excitation levels. One may conclude that in many cases describing functions for impedance or reflection coefficient characterize the nonlinear response of resonators with acceptable accuracy.

Appendix

The solver validation in the nonlinear regime is presented using impedance describing function measurements performed by M. A. Temiz[39] from TU Eindhoven on configuration HRS in a frequency range $[100, 700]$ Hz corresponding to $\tilde{\omega}_0 \in [0.27, 1.87]$. Figure 7 shows the normalized impedance and the reflection coefficient for an overall SPL of $120\,\mathrm{dB}$ and $125\,\mathrm{dB}$ obtained by the measurements and the CFD simulations. In those simulations, the input amplitudes of the f wave have been set in a way that the acoustic SPL directly in front of neck matches the target value. Since the nonlinear effects affect mainly the resistance $\Re(z)$, it is more challenging to capture this quantity correctly in the CFD simulation, see
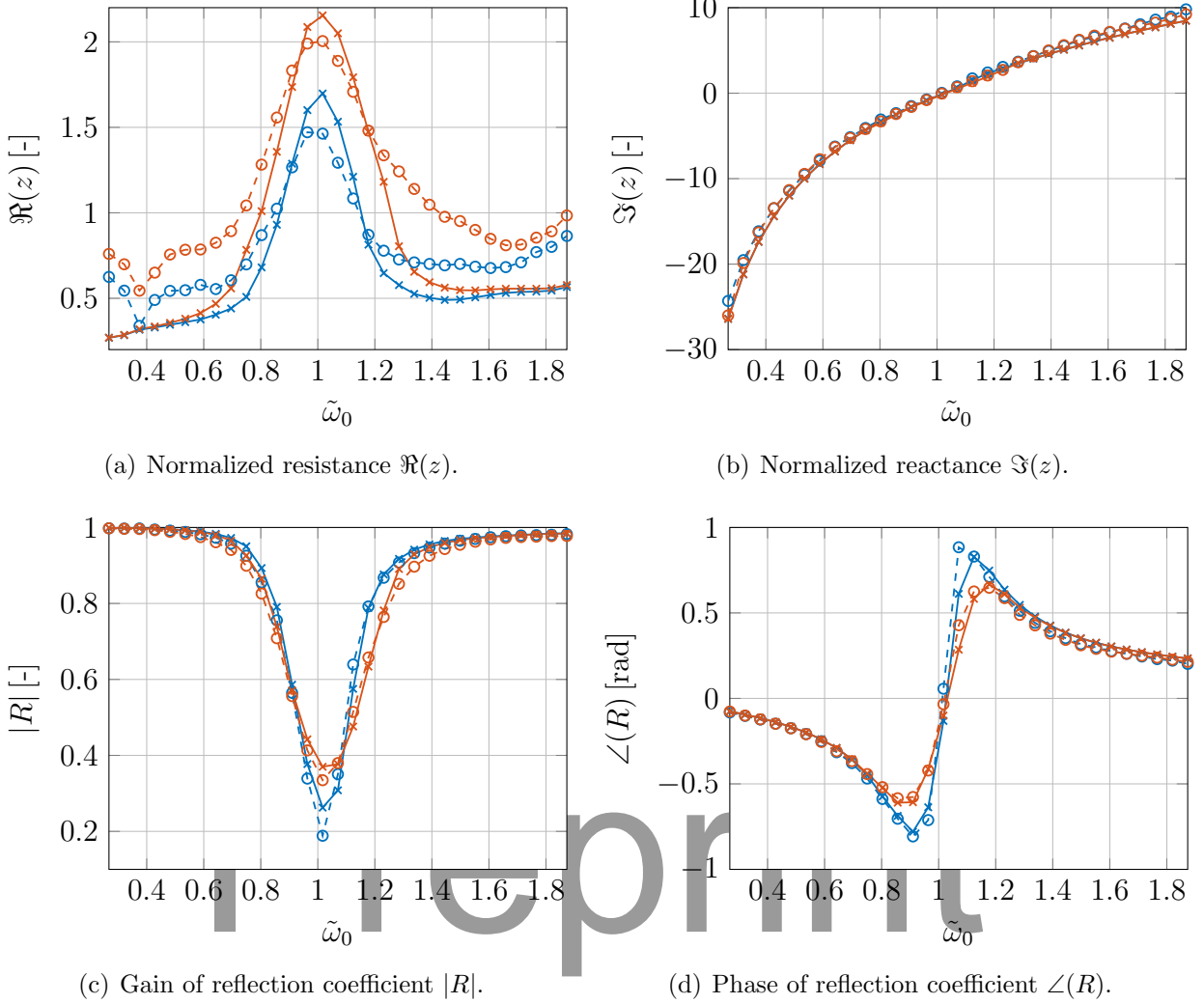
(a) Normalized resistance $\Re(z)$.

(b) Normalized reactance $\Im(z)$.

(c) Gain of reflection coefficient $|R|$.

(d) Phase of reflection coefficient $\angle(R)$.

Figure 7. Impedance and reflection coefficient for HRS determined by LES and measurements of M. A. Temiz [39] at a SPLs of 120 dB (LES: - ⊙ -, measurements: —×—) and 125 dB (LES: - ⊙ -, measurements: —×—).

Fig 7(a), than the reactance $\Im(z)$, which always fits very accurately, see Fig 7(b). The curves agree quite reasonably but the numerics slightly over-predicts the nonlinear resistance. A reason for this is (at least partially) that the edges in the CFD mesh are perfectly sharp while the real sample is not due to manufacturing reasons [20]. The measurements are also a bit shaky away from the eigenfrequency. This shaky behavior does not originate from physics but from the ill-conditioned transformation from reflection coefficient to resistance. The reflection coefficient is in both experiment and CFD the quantity that is directly and subsequently transformed to the impedance. Thus, a comparison in the reflection coefficient is more suitable. This is depicted in Figs. 7(c) and 7(d). Here, the curve match is almost perfect and shows the quality of the computational setup.

Acknowledgments

References

[1] *The Jet Engine.* Rolls-Royce Ltd., Derby, U.K., 5th edition, 1996. ISBN 0902121 235.

[2] V. Bellucci, P. Flohr, C. O. Paschereit, and F. Magni. On the Use of Helmholtz Resonators for Damping Acoustic Pulsations in Industrial Gas Turbines. *J. Eng. Gas Turbines Power*, 126(2):271–275, 2004. doi: 10.1115/1.1473152.

[3] K. Förner, A. Cárdenas Miranda, and W. Polifke. Mapping the Influence of Acoustic Resonators on Rocket Engine Combustion Stability. *J. Propuls. Power*, 31(4):1159–1166, 2015. doi: 10.2514/1.B35660.

[4] C. H. Sohn and J. H. Park. A Comparative Study on Acoustic Damping Induced by Half-Wave, Quarter-Wave, and Helmholtz Resonators. *Aerospace Science and Technology*, 15 (8):606–614, 2011. doi: 10.1016/j.ast.2010.12.004.

[5] M. G. Jones, M. B. Tracy, W. R. Watson, and T. L. Parrott. Effects of Liner Geometry on Acoustic Impedance. In *8th AIAA/CEAS Aeroacoustics Conference & Exhibit*, Breckenridge, Colorado, U.S.A., 2002. doi: 10.2514/6.2002-2446.

[6] Q. Zhang and D. J. Bodony. Numerical Investigation of a Honeycomb Liner Grazed by Laminar and Turbulent Boundary Layers. *J. Fluid Mech.*, 792:936–980, 2016. doi: 10.1017/jfm.2016.79.

[7] J. D. Eldredge and A. P. Dowling. The Absorption of Axial Acoustic Waves by a Perforated Liner with Bias Flow. *J. Fluid Mech.*, 485:307–335, 2003. doi: 10.1017/S0022112003004518.

8 V. Bellucci, P. Flohr, and C. O. Paschereit. Numerical and Experimental Study of Acoustic Damping Generated by Perforated Screens. *AIAA J.*, 42(8):1543–1549, 2004. doi: 10.2514/1.9841.

9 A. Scarpato, S. Ducruix, and T. Schuller. Optimal and off-design operations of acoustic dampers using perforated plates backed by a cavity. *J. Sound Vib.*, 332(20):4856–4875, 2013. doi: 10.1016/j.jsv.2013.03.030.

10 B. Ćosić, T. G. Reichel, and C. O. Paschereit. Acoustic Response of a Helmholtz Resonator Exposed to Hot-Gas Penetration and High Amplitude Oscillations. *J. Eng. Gas Turbines Power*, 134(10):101503–101503, 2012.

11 J. Rupp, G. Peacock, G. Regunath, and J. Carrotte. Assessment and Prediction of Helmholtz Resonator Performance Within Gas Turbine Combustion Systems. In *ASME Turbo Expo 2014*, Düsseldorf, Germany, 2014. doi: 10.1115/GT2014-26907.

12 C. K. W. Tam and K. A. Kurbatskii. Microfluid Dynamics and Acoustics of Resonant Liners. *AIAA J.*, 38(8):1331–1339, 2000. doi: 10.2514/2.1132.

13 C. K. W. Tam, H. Ju, and B. E. Walker. Numerical Simulation of a Slit Resonator in a Grazing Flow Under Acoustic Excitation. *J. Sound Vib.*, 313(3–5):449 – 471, 2008. doi: 10.1016/j.jsv.2007.12.018.

14 C. K. W. Tam, H. Ju, M. G. Jones, W. R. Watson, and T. L. Parrott. A Computational and Experimental Study of Resonators in Three Dimensions. *J. Sound Vib.*, 329(24): 5164–5193, 2010. doi: 10.1016/j.jsv.2010.06.005.

15 Q. Zhang and D. J. Bodony. Numerical Investigation and Modelling of Acoustically Excited Flow Through a Circular Orifice Backed by a Hexagonal Cavity. *J. Fluid Mech.*, 693:367–401, 2012. doi: 10.1017/jfm.2011.537.

16 Q. Zhang and D. J. Bodony. Direct Numerical Investigation of Acoustic Liners with Single and Multiple Orifices Grazed by a Mach 0.5 Boundary Layer. Washington, D.C., U.S.A., 2016. American Institute of Aeronautics and Astronautics. doi: 10.2514/6.2016-3626.

17 S. Mendez and J. D. Eldredge. Acoustic Modeling of Perforated Plates with Bias Flow for Large-Eddy Simulations. *J. Comput. Phys.*, 228(13):4757–4772, 2009. doi: 10.1016/j.jcp.2009.03.026.

18 J. Tournadre, W. Desmet, and P. Martínez-Lera. Evaluation of Temperature Effects on Passive Acoustic Dampers with a Frequency-Domain Linearized Navier-Stokes Equations

Solver. Athens, Greece, 07/1/16. URL http://iiav.org/archives_icsv_last/2016_icsv23/content/papers/papers/full_paper_857_20160523171052430.pdf.

[19] C. Ji and D. Zhao. Lattice Boltzmann Investigation of Acoustic Damping Mechanism and Performance of an in-Duct Circular Orifice. *J. Acoust. Soc. Am.*, 135(6):3243–3251, 2014. doi: 10.1121/1.4876376.

[20] J. Tournadre, K. Förner, W. Polifke, P. Martínez-Lera, and W. Desmet. Determination of Acoustic Impedance for Helmholtz Resonators Through Incompressible Unsteady Flow Simulations. In *22nd AIAA/CEAS Aeroacoustics Conference*, Lyon, France, 2016. doi: 10.2514/6.2016-2917.

[21] U. Ingard. On the Theory and Design of Acoustic Resonators. *J. Acoust. Soc. Am.*, 25 (6), 1953. doi: 10.1121/1.1907235.

[22] U. Ingard and H. Ising. Acoustic Nonlinearity of an Orifice. *J. Acoust. Soc. Am.*, 42(1): 6–17, 1967. doi: 10.1121/1.1910576.

[23] T. H. Melling. The Acoustic Impedance of Perforates at Medium and High Sound Pressure Levels. *J. Sound Vib.*, 29(1):1–65, 1973. doi: 10.1016/S0022-460X(73)80125-7.

[24] A. Cummings. Transient and Multiple Frequency Sound Transmission Through Perforated Plates at High Amplitude. *J. Acoust. Soc. Am.*, 79(4):942–951, 1986. doi: 10.1121/1.393691.

[25] A. S. Hersh, B. E. Walker, and J. W. Celano. Helmholtz Resonator Impedance Model, Part 1: Nonlinear Behavior. *AIAA J.*, 41(5):795–808, 2003. doi: 10.2514/2.2041.

[26] D. K. Singh and S. W. Rienstra. Nonlinear Asymptotic Impedance Model for a Helmholtz Resonator Liner. *J. Sound Vib.*, 333(15):3536–3549, 2014. doi: 10.1016/j.jsv.2014.03.013.

[27] J. H. M. Disselhorst and L. V. Wijngaarden. Flow in the exit of open pipes during acoustic resonance. *J. Fluid Mech.*, 99(02):293–319, 1980. doi: 10.1017/S0022112080000626.

[28] M. Atig, J.-P. Dalmont, and J. Gilbert. Termination Impedance of Open-Ended Cylindrical Tubes at High Sound Pressure Level. *Comptes Rendus L'Académie Sci. Sér. IIb Mécanique*, 332(4):299–304, 2004. doi: 10.1016/j.crme.2004.02.008.

[29] M. A. Temiz, J. Tournadre, I. Lopez Arteaga, P. Martınez-Lera, and A. Hirschberg. Effect of Orifice Geometry on the Non-Linear Acoustic Resistance of Perforated Plates in the Transition Regime. Florence, Italy, 2015. URL http://iiav.org/archives_icsv_last/2015_icsv22/content/papers/papers/full_paper_1014_20150315164202977.pdf.

[30] E. Laudien, R. Pongratz, R. Piero, and D. Preclick. Fundamental Mechanisms of Combustion Instabilities: Experimental Procedures Aiding the Design of Acoustic Cavities. In *Liquid Rocket Engine Combustion Instability*, Progress in Astronautics and Aeronautics, pages 377–399. American Institute of Aeronautics and Astronautics, 1995. ISBN 978-1-56347-183-4.

[31] K. Förner, M. A. Temiz, W. Polifke, I. Lopez Arteaga, and A. Hirschberg. On the Non-Linear Influence of the Edge Geometry on Vortex Shedding in Helmholtz Resonators. In *22nd International Congress on Sound and Vibration (ICSV22)*, Florence, Italy, 2015. URL http://iiav.org/archives_icsv_last/2015_icsv22/content/papers/papers/full_paper_1341_20150325133515128.pdf.

[32] U. Ingard. Nonlinear Distortion of Sound Transmitted through an Orifice. *J. Acoust. Soc. Am.*, 48(1A):32–33, 1970. doi: 10.1121/1.1912106.

[33] S. W. Rienstra and A. Hirschberg. An Introduction to Acoustics. Technical Report IWDE 92-06, Eindhoven University of Technology, 2015. URL http://www.win.tue.nl/~sjoerdr/papers/boek.pdf.

[34] H. Bodén and L. Zhou. An Experimental Study of the Effect of Flow and High Level Acoustic Excitation on the Acoustic Properties of Perforates and Orifices. In *20th International Congress on Sound and Vibration (ICSV20)*, Bangkok, Thailand, 2013.

[35] Q. Zhang and D. J. Bodony. Effects of the Turbulent Grazing Flow Over the Impedance Prediction of a Single-Orifice Helmholtz Resonator. In *22nd AIAA/CEAS Aeroacoustics Conference*, Lyon, France, 2016. American Institute of Aeronautics and Astronautics. doi: 10.2514/6.2016-2729.

[36] R. D. Blevins. *Applied Fluid Dynamics Handbook*. Van Nostrand Reinhold, NY, U.S.A., 1984. ISBN 0-442-21296-8.

[37] OpenFOAM Foundation. OpenFOAM (Version 2.3.0) [software]. 2014.

[38] T. Poinsot and S. K. Lele. Boundary Conditions for Direct Simulation of Compressible Viscous Flows. *J. Comp. Phys.*, 101(1):104–129, 1992. doi: 10.1016/0021-9991(92)90046-2.

[39] M. A. Temiz. Private Measurement Data Exchange. 2016.

[40] A. Mages. *Numerische Untersuchung Des Akustischen Nichtlinearen Dämpfungsverhaltens von Perforierten Platten Und Helmholtzresonatoren*. Bachelor thesis, TU München, Garching, Germany, 2016. URL https://mediatum.ub.tum.de/node?id=1291369.

[41] H. Bodén. Acoustic Properties of Perforates Under High Level Multi-Tone Excitation. In *19th AIAA/CEAS Aeroacoustics Conference*, Berlin, Germany, 2013. doi: 10.2514/6. 2013-2175.

Preprint